Environmental Science Advances

Accepted Manuscript

Published on 27 July 2026

This is an Accepted Manuscript, which has been through the Royal Society of Chemistry peer review process and has been accepted for publication.

Accepted Manuscripts are published online shortly after acceptance, before technical editing, formatting and proof reading. Using this free service, authors can make their results available to the community, in citable form, before we publish the edited article. We will replace this Accepted Manuscript with the edited and formatted Advance Article as soon as it is available.

You can find more information about Accepted Manuscripts in the Information for Authors.

Please note that technical editing may introduce minor changes to the text and/or graphics, which may alter content. The journal's standard Terms & Conditions and the Ethical guidelines still apply. In no event shall the Royal Society of Chemistry be held responsible for any errors or omissions in this Accepted Manuscript or any consequences arising from the use of any information it contains.

ROYAL SOCIETY OF CHEMISTRY

rsc.li/esadvances

Atmospheric sulfate aerosols influence climate, air quality, and cloud formation, yet they are often represented in models as composition-independent, fully liquid particles. This study shows that common sulfate cations can strongly alter aerosol density, hygroscopic growth, refractive index, and phase state. In particular, multivalent sulfates form highly viscous, gel-like particles under dry conditions, suppressing water transport while modifying shortwave radiative forcing. These measurements and the bulk–droplet equivalency framework provide experimentally constrained parameters for more realistic treatment of sulfate aerosols in climate and atmospheric chemistry models. The results are also relevant to evaluating the environmental implications of sulfate-based geoengineering materials.

Cation Identity, Phase State, and Density as Key Determinants of Radiative Forcing in Atmospheric Sulfate Systems

Vahid Shahabadi,[†] Yingshi Luo,[‡] Aaron M. Palmisano,[¶] Pedro De Allende,[¶] Alison Bain,[§] James F. Davies,[¶] and Thomas C. Preston[*,†,‡]

[†]*Department of Atmospheric and Oceanic Sciences, McGill University, Montreal, QC, H3A 0B9, Canada*

[‡]*Department of Chemistry, McGill University, Montreal, QC, H3A 0B8, Canada*

[¶]*Department of Chemistry, University of California Riverside, CA, 92521 USA*

[§]*Department of Chemistry, Oregon State University, Corvallis, OR, 97331, USA*

E-mail: thomas.preston@mcgill.ca

Abstract

Sulfate aerosols strongly influence climate through aerosol–radiation and aerosol–cloud interactions and are widely considered for climate mitigation strategies. Despite this relevance, sulfate aerosols are commonly represented using simplified assumptions based on the binary H_2SO_4–H_2O system and a composition-independent refractive index. Here, we show that cation identity, phase state, and density can substantially alter the optical properties of sulfate aerosols and the extent to which their evolution is governed by diffusion-limited mass transport. We combine bulk measurements of density, water activity, and refractive index with single-particle optical trapping and electrodynamic balance experiments to quantify droplet size, radial growth factors, and

wavelength-dependent refractive indices. This approach is applied to seven inorganic sulfates (Li_2SO_4, Na_2SO_4, K_2SO_4, $(NH_4)_2SO_4$, $MgSO_4$, $Al_2(SO_4)_3$, and $MnSO_4$) and two short-chain organosulfates. We further introduce a bulk–droplet equivalency framework that retrieves the droplet thermodynamic state (e.g., composition and water activity, including metastable and supersaturated regimes) directly from levitated-droplet measurements. Multivalent sulfates, specifically $MgSO_4$, $MnSO_4$, and $Al_2(SO_4)_3$, exhibit pronounced inflection points and hysteresis. These features are consistent with a transition to highly viscous, gel-like phases at relative humidity (RH) $\approx$ 35–40 %. In this low-RH regime, these systems display humidity-buffered behavior, in which density, refractive index, and growth factor vary only weakly with further decreases in humidity, strongly suppressing water transport and likely reducing heterogeneous reactivity. Elevated refractive indices at 589 nm, reaching $\sim$ 1.49 for $MgSO_4$ and $Al_2(SO_4)_3$ and $\sim$ 1.53 for $MnSO_4$, yield enhanced shortwave radiative forcing efficiencies relative to conventional sulfate, as shown using Mie scattering and one-dimensional radiative transfer calculations (libRadtran/DISORT) for lognormal size distributions. These results highlight the importance of cation-specific phase behavior and optical properties for accurately representing sulfate aerosols in climate, atmospheric chemistry models, and geoengineering proposals.

1 Introduction

Sulfate aerosols are efficient scatterers of sunlight and serve as a canonical example of negative aerosol direct radiative forcing, as large volcanic injections of sulfur dioxide (SO_2) into the stratosphere naturally demonstrate sulfate's capacity to perturb Earth's radiation balance and climate on short timescales.[1,2] In addition, they provide reactive surfaces for heterogeneous chemistry (e.g., acid-catalyzed reactions that contribute to secondary organic aerosol formation), thereby altering oxidant budgets and particle growth pathways. Sulfate-containing particles can also deactivate ice nucleation under certain conditions, modifying cloud phase and lifetime.[3–7] Furthermore, they act as cloud condensation nuclei (CCN), in-

creasing cloud droplet number concentrations and cloud reflectivity (the Twomey effect). Observational and modeling studies indicate that sulfate aerosols remain a major source of uncertainty in estimates of anthropogenic radiative forcing.[8–11]

Sulfate forms in the atmosphere via oxidation of sulfur precursors such as SO_2 and dimethyl sulfide (DMS), originating from both anthropogenic and natural sources.[12–14] Gas-phase oxidation and aqueous-phase reactions within clouds and droplets convert these precursors into particulate sulfate.[15–17] Biogenic emissions, particularly DMS oxidation, constitute a major natural sulfate source, while aqueous-phase and surface-catalyzed oxidation pathways regulate sulfate production rates and mixing state, thereby controlling regional sulfate mass loading and chemical composition.[3,18] The chemical processing and mixing state of sulfate with other aerosol components modify its solubility, hygroscopicity, and optical properties.[19,20]

The magnitude of aerosol indirect effects depends on how microphysical and optical properties respond to ambient humidity. Classical theory predicts that increasing the concentration of soluble particles produces more numerous but smaller cloud droplets for a fixed liquid water content, enhancing cloud albedo, known as the Twomey effect.[8,21,22] The efficacy of this mechanism depends on hygroscopic growth, water activity, density, and refractive index (RI) as functions of relative humidity (RH). Even small variations in these properties can modify activation barriers (the free-energy barrier to droplet activation and growth) and scattering characteristics, thereby influencing cloud reflectivity and lifetime,[11,23,24] with higher solute concentration and density lowering water activity and tending to increase this barrier, whereas reduced surface tension decreases it. Yang et al. simulated a global mean sulfate direct radiative forcing (DRF) of -0.42 W m^{-2} relative to a state with no sulfur emissions. In a separate sensitivity experiment, they quantified the sulfate incremental indirect radiative forcing (IRF) as the change in cloud radiative forcing between their control simulation and a simulation with a uniform 20% reduction in global sulfur emissions (SO_2, sulfate, and DMS), yielding -0.44 W m^{-2}, with DMS contributing -0.23 W m^{-2}. These two values rep-

resent different forcing definitions and experimental baselines and are therefore not directly comparable.[24]

The binary $H_2SO_4-H_2O$ system is often used as a proxy for sulfate aerosols in atmospheric studies. This representation effectively neglects the presence and influence of inorganic cations that are ubiquitous in real atmospheric sulfate particles. In marine environments, sea spray aerosols contribute substantial amounts of sodium (Na^+); however, ions such as potassium (K^+), magnesium (Mg^{2+}), and calcium (Ca^{2+}) are often emitted with enrichment factors comparable to or exceeding that of Na^+. Notably, based on the composition of seawater, the mass fraction of Mg^{2+} in sea salt (0.0396) is comparable to that of sulfate itself (0.0768).[4] Measurements of nascent sea spray aerosol are consistent with this, with seawater mass ratios of $Mg^{2+}/Na^+ = 0.12$ and $SO_4^{2-}/Na^+ = 0.26$.[25] Beyond marine sources, metals, including aluminum (Al) and manganese (Mn), are efficiently introduced into the atmosphere via mineral dust emissions. Aluminum alone can account for up to approximately 10% of total dust mass, corresponding to a global annual emission of order 3 Tg.[26,27] Mn, a highly water-soluble species, has been shown to catalyze heterogeneous reactions that accelerate the oxidation of sulfur dioxide on aerosol surfaces during haze events.[28] Moreover, recent work demonstrates that the solubility of Al in atmospheric particles can be significantly enhanced through chemical aging processes associated with aerosol acidification.[29] Taken together, these observations indicate that the exclusion of cation effects represents a nontrivial limitation in simplified sulfate aerosol frameworks and that a more explicit treatment of cation chemistry is essential for accurately describing sulfate aerosol properties.

Despite extensive measurements for some systems, substantial gaps remain. Many sulfate systems lack datasets spanning both bulk and droplet phases across the wide humidity and concentration ranges needed for accurate atmospheric modeling. Data for RI, density, and water activity at high solute mass fractions or low RH are often limited, and polynomial fits are frequently used to estimate these quantities.[30] Intercomparisons of different single-particle methods under identical conditions are scarce. Moreover, experimentally validated

frameworks for linking droplet-scale properties to bulk parameterizations remain limited, making it difficult to rigorously validate polynomial or mixing models across metastable regimes. Finally, radiative forcing modification associated with the existence of cations in atmospheric sulfate aerosols has not been constrained, leaving major uncertainties in current estimates.

To address these gaps, we conduct a systematic study linking bulk solution measurements to droplet behavior using complementary optical trapping (OT) and linear quadrupole electrodynamic balance (EDB) methods. We measure density, water activity, RI, solute mass fraction, and concentration in bulk solutions, and record droplet size and optical properties under controlled RH. We develop a bulk–droplet equivalency (BDE) framework to bridge bulk and droplet phases, enabling retrieval of these quantities, along with the radial growth factor, directly from levitated-droplet measurements. This framework extends to metastable regimes where droplets become supersaturated, allowing comparison with second-order polynomial parameterizations fitted to bulk data. An oscillator-based RI model is used to cross-validate retrieved indices. These results show that sulfate aerosol hygroscopicity and optical properties can vary strongly with cation identity and phase state, and that droplet-based constraints are needed to represent these effects in models beyond simple equilibrium, composition-averaged parameterizations. Finally, we use these experimentally derived properties to calculate shortwave radiative forcing efficiencies under stratospherically relevant dry conditions and size distributions, and we discuss how gel formation, longwave absorption uncertainty, supply-chain scalability, and heterogeneous reactivity together shape the suitability of multivalent sulfates as candidate materials for stratospheric aerosol injection (SAI).

Using the BDE framework, we show that cation identity and phase state are primary controls on the physical chemistry of these aerosols in highly concentrated, supersaturated regimes. At low relative humidity (RH < 35 to 40%), the multivalent sulfate droplets $MgSO_4$, $MnSO_4$, and $Al_2(SO_4)_3$ transition into a highly viscous, gel-like state with refractive indices of $\sim$1.49 to 1.53, higher than the $\sim$1.43 of the binary H_2SO_4–H_2O baseline commonly assumed

for stratospheric sulfate. Shortwave radiative transfer calculations with libRadtran/DISORT indicate that this optical difference corresponds to an increase in shortwave radiative forcing efficiency of about 5%, while more importantly, the gel state also imposes diffusion limitations that strongly retard water transport and are expected to reduce heterogeneous reactivity.

2 Materials and Methods

2.1 Materials

We investigated seven inorganic sulfate salts: lithium sulfate (Sigma, 99.5%, UK), sodium sulfate (Sigma, 99%, India), potassium sulfate (Sigma, 99%, China), magnesium sulfate (Sigma, 99%, Japan), ammonium sulfate (Sigma, 99%, France), aluminum sulfate (Sigma, 99%, US), and manganese sulfate (MP Biomedicals, 99%, India), as well as two short-chain organosulfates, sodium methyl sulfate (SMS, Sigma, 93%, US) and sodium ethyl sulfate (SES, Sigma, 98%, Japan). All solutions were prepared from powders as received (no further purification) using deionized water and were diluted to the desired concentrations by serial dilution. To minimize hydrolysis, aluminum sulfate was dissolved in water pre-acidified to pH $\approx$ 2.5 using sulfuric acid. Fully transparent solutions of aluminum sulfate were obtained after $\approx$ 10 days. See Section 1 of the Supplementary Information for additional details.

2.2 Bulk–Droplet Equivalency (BDE)

For a solution containing N components, the mass density ρ can be written in terms of the partial specific volumes $\bar{\mathrm{v}}_\alpha$ and mass fractions w_α of each component α as

$$\frac{1}{\rho} = \sum_{\alpha=1}^{N} \bar{\mathrm{v}}_\alpha w_\alpha. \tag{1}$$

For the binary aqueous solutions considered here (solute s and water w), Eq. 1 reduces to

$$\frac{1}{\rho} = \bar{\mathrm{v}}_\mathrm{s}\, w_\mathrm{s} + \bar{\mathrm{v}}_\mathrm{w}\,(1 - w_\mathrm{s}), \tag{2}$$

where w_s is the solute mass fraction. In the BDE framework, we take Eq. 2 as the statement of volume additivity and assume the water partial specific volume remains close to that of pure water, $\bar{\mathrm{v}}_\mathrm{w} \approx 1/\rho_\mathrm{w}$, where ρ_w is the density of pure water. Under this approximation, the droplet volume change upon water loss is given by the volume of pure water removed.

We establish an initial reference state (subscript "i") by holding a droplet at a known relative humidity, for which water activity $a_\mathrm{w} = \mathrm{RH}/100\,\%$ (neglecting the Kelvin effect, which is justified for the micron-sized droplets studied here). If the droplet's measured refractive index matches that of a bulk solution at the same a_w, we assume the droplet shares the same thermodynamic properties as that bulk reference. This matching condition defines a compositional equivalence: the droplet and bulk solution are assumed to have identical chemical composition at the same water activity, and no additional dilution or compositional adjustment is introduced. We use a superscript $\circ$ to indicate quantities obtained from the bulk calibration. Thus, ρ_i°, $w_\mathrm{s,i}^\circ$, and $C_\mathrm{s,i}^\circ$ denote the droplet density, solute mass fraction, and solute molarity at the reference state, all known from the bulk calibration. The corresponding droplet radius at the reference state, R_i, is measured, giving an initial volume of $V_\mathrm{i} = (4\pi/3)R_\mathrm{i}^3$ and initial mass of $m_\mathrm{i} = \rho_\mathrm{i}^\circ V_\mathrm{i}$.

For a nonvolatile solute, its mass in the droplet is conserved during water uptake or loss. Using the calibrated reference composition, the solute mass is therefore fixed at $m_\mathrm{s} = w_\mathrm{s,i}^\circ\, m_\mathrm{i}$. Upon lowering RH, water evaporates and the droplet radius decreases to R_f ($< R_\mathrm{i}$), and the droplet will often enter a supersaturated state. The final droplet volume, V_f, is obtained from the measured radius, R_f. Therefore the change in droplet volume is

$$\Delta V = V_\mathrm{i} - V_\mathrm{f} = \frac{4}{3}\pi\left(R_\mathrm{i}^3 - R_\mathrm{f}^3\right). \tag{3}$$

With $\bar{v}_w \approx 1/\rho_w$, the droplet mass change is approximated as the mass of pure water removed,

$$\Delta m = m_i - m_f = \rho_w \Delta V, \tag{4}$$

where m_f is the final mass of the droplet and the only unknown in Equation 4. Therefore it will be $m_f = m_i - \rho_w \Delta V$ and, because m_s is conserved, the final solute mass fraction follows directly from mass balance,

$$w_{s,f} = \frac{m_s}{m_f} = \frac{m_i}{m_f} w^\circ_{s,i}. \tag{5}$$

The final droplet density is then obtained from its definition, $\rho_f = m_f/V_f$, and the solute concentration in molarity is $C_f = m_s/(M_s V_f)$, where M_s is the solute molar mass.

Finally, the dry particle volume is $V_{dry} = m_s/\rho_s$, where ρ_s is the density of the dry solute. The corresponding dry-equivalent radius is

$$R_{dry} = \left(\frac{3V_{dry}}{4\pi}\right)^{1/3}, \tag{6}$$

and the radial growth factor is

$$\mathrm{rGF} = \frac{R(\mathrm{RH})}{R_{dry}}. \tag{7}$$

Application of the reference-state mass balance ($m_s = w^\circ_{s,i}\,\rho^\circ_i V_i$ with $V_i = (4\pi/3)R_i^3$) to Eq. 6 yields a closed-form expression for R_{dry} in terms of bulk-calibrated reference properties and the measured reference radius,

$$R_{dry} = R_i \left(\frac{w^\circ_{s,i}\,\rho^\circ_i}{\rho_s}\right)^{1/3}. \tag{8}$$

To validate the accuracy of the BDE framework, we used aqueous $CaCl_2$ as a benchmark system because it accesses very low water activities ($a_w \approx 0.2$), providing a stringent test over a wide thermodynamic range. Thermodynamic properties retrieved from BDE analysis of levitated droplets were compared directly against independent bulk measurements over

the overlapping a_w range. A detailed evaluation of this validation is provided in Section 2 of the Supplementary Information.

In the subsequent sections, we use two models for the thermodynamic properties of the chosen sulfate systems. One is a common quadratic model to estimate the solution density at high concentrations. The details regarding this model are provided in Section 3 of the Supplementary Information. The second model is an effective oscillator model that provides fitting parametrization for the refractive index as a function of both concentration and wavelength. The details of this model are provided in Section 4 of the Supplementary Information.

2.3 Single Droplet Measurements

We employed two complementary single-droplet levitation techniques, optical trapping (OT) and linear-quadrupole electrodynamic balance (EDB), to study hygroscopic behavior and RI evolution of aqueous sulfate particles over a wide RH range. Figure 1(a,b) illustrates the schematic of the setups. By analyzing the morphology dependent resonances (MDRs) in the inelastic Raman scattering from the trapped droplet at dry and wet conditions, we can extract the size and the RI of the droplet, as depicted in Figure 1(c,d). Details regarding these two methods are provided in Section 5.1 and Section 5.2 of the Supplementary Information.

2.4 Bulk Measurements

Table 1 summarizes the measured physicochemical properties of the sulfate systems. With increasing solute mass fraction, all systems show increasing density and refractive index, together with decreasing water activity, consistent with higher solute loading and stronger solute-solvent interactions. Among the inorganic salts, magnesium, aluminum, and manganese sulfates exhibit comparatively steep increases in both density and refractive index with increasing concentration, likely reflecting increasingly structured hydration environments and the approach to highly viscous or gel-like regimes. Potassium sulfate, by contrast, shows more modest changes over the accessible range, consistent with its limited solubility,

Table 1: Bulk physicochemical properties of aqueous sulfate salt solutions at $T = 294 \pm 1$ K. Listed values correspond to the indicated solution concentration. Bulk solubility limits for Li_2SO_4, Na_2SO_4, K_2SO_4, $(NH_4)_2SO_4$, $MgSO_4$, and $Al_2(SO_4)_3$ are taken from Ref. 31, for $MnSO_4$ is taken from Ref. 32, and for SMS and SES are taken from Ref. 33.

Solute	**Molar Mass (g mol^{-1})**	**Solubility (g/100 g H_2O)**	**Concentration (M)**	**Mass Fraction**	**Density (g cm^{-3})**	**Water Activity**	**Refractive Index (589 nm)**
Li_2SO_4	109.94	34.2	0.50	0.0523	1.0495	0.9853	1.3417
			1.00	0.1008	1.0901	0.9624	1.3505
			1.50	0.1457	1.1317	0.9346	1.3581
			2.00	0.1880	1.1707	0.9039	1.3655
			2.50	0.2275	1.2084	0.8679	1.3726
Na_2SO_4	142.04	28.1	0.25	0.0356	1.0301	0.9951	1.3350
			0.50	0.0694	1.0605	0.9890	1.3403
			0.75	0.1018	1.0950	0.9760	1.3475
			1.00	0.1329	1.1231	0.9694	1.3515
			1.25	0.1599	1.1434	0.9650	1.3553
			1.53	0.1878	1.1788	0.9534	1.3606
			1.70	0.2089	1.1900	0.9450	1.3627
K_2SO_4	174.26	12.0	0.10	0.0171	1.0185	0.9976	1.3344
			0.50	0.0822	1.0597	0.9879	1.3408
			0.63	0.1263	1.0886	0.9788	1.3457
$(NH_4)_2SO_4$	132.14	76.4	0.50	0.0650	1.0400	0.9821	1.3445
			1.00	0.1050	1.0780	0.9710	1.3524
			1.50	0.1650	1.1010	0.9523	1.3623
			2.00	0.2320	1.1380	0.9282	1.3696
			2.50	0.2840	1.1635	0.9027	1.3770
			3.00	0.3316	1.1954	0.8747	1.3852
			3.50	0.3788	1.2207	0.8411	1.3926
			4.00	0.4225	1.2502	0.8043	1.4000
$MgSO_4$	120.37	35.7	0.50	0.0599	1.0740	0.9923	1.3445
			1.00	0.1134	1.1308	0.9812	1.3550
			1.50	0.1625	1.1796	0.9697	1.3650
			2.00	0.2088	1.2177	0.9499	1.3740
			2.50	0.2473	1.2699	0.9266	1.3810
$MnSO_4$	151.00	64.3	0.50	0.0782	1.0800	0.9900	1.3456
			1.00	0.1474	1.1440	0.9830	1.3600
			1.50	0.2072	1.2160	0.9690	1.3734
			2.00	0.2618	1.2880	0.9500	1.3843
			2.50	0.3127	1.3500	0.9150	1.3957
			3.00	0.3618	1.4000	0.8790	1.4050
			3.50	0.4020	1.4680	0.8359	1.4135
$Al_2(SO_4)_3$	342.15	38.5	0.25	0.0792	1.0804	0.9731	1.3515
			0.50	0.1409	1.1609	0.9500	1.3680
			0.75	0.2113	1.2466	0.9150	1.3825
			0.94	0.2550	1.3050	0.8600	1.3935
SMS	134.09	61.8	0.50	0.0700	1.0250	0.9821	1.3384
			1.00	0.1300	1.0720	0.9636	1.3436
			1.50	0.1800	1.1050	0.9455	1.3474
			2.00	0.2400	1.1520	0.9222	1.3526
			2.50	0.2900	1.1840	0.8962	1.3572
			3.00	0.3400	1.2220	0.8664	1.3610
			3.50	0.3800	1.2560	0.8334	1.3662
SES	148.11	127.9	0.50	0.0700	1.0300	0.9833	1.3391
			1.00	0.1400	1.0540	0.9710	1.3444
			1.50	0.2000	1.0990	0.9418	1.3503
			2.00	0.2600	1.1320	0.9124	1.3564
			2.50	0.3200	1.1540	0.8837	1.3590
			3.00	0.3700	1.1970	0.8505	1.3626
			3.50	0.4300	1.2160	0.8154	1.3670

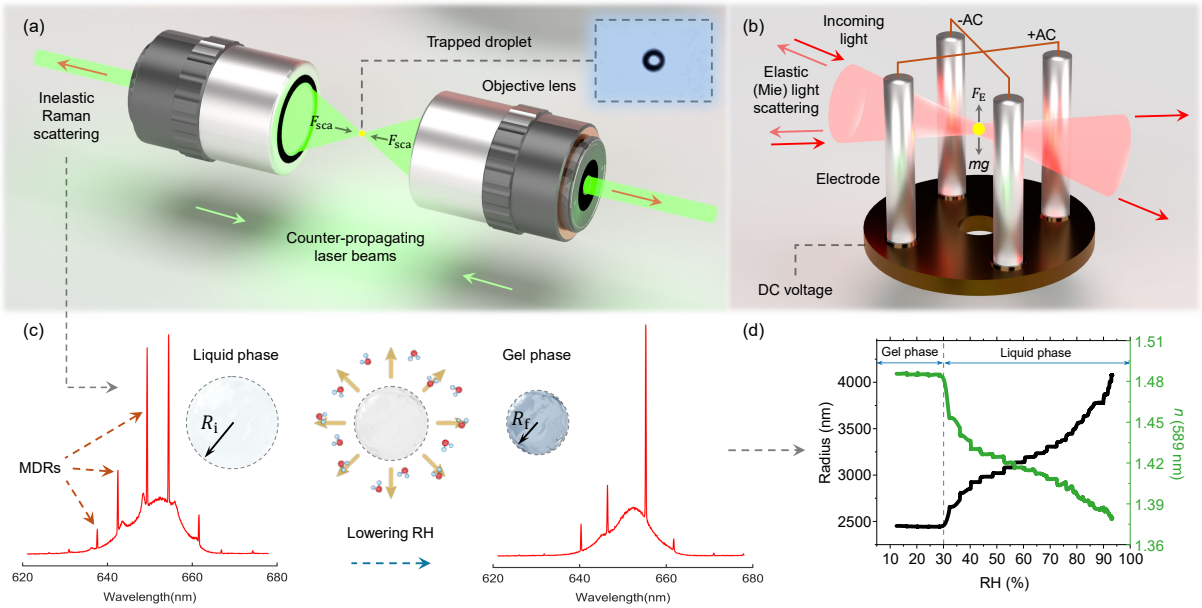

Figure 1: Schematic presentation of (a) optical trapping (OT) and (b) linear quadrupole electrodynamic balance (EDB) single-particle investigation techniques. (c) Change in cavity-enhanced Raman scattering (CERS) for a liquid droplet as RH is lowered, culminating in the formation of a gel-phase particle. Morphology-dependent resonances (MDRs) are the sharp resonance peaks that appear at the top of the spectrum. (d) A typical size and refractive index evolution during droplet water loss induced by decreasing RH.

while ammonium sulfate reaches particularly low water activities and elevated refractive indices at high concentrations, reflecting its ability to form highly concentrated aqueous aerosol under atmospherically relevant RH. The organosulfates SMS and SES show weaker concentration dependencies in both density and refractive index than the multivalent inorganic salts, and their solutions are systematically less dense, consistent with their partial organic character. Details regarding the measurements are provided in Section 5.3 of the Supplementary Information.

3 Results and Discussion

3.1 Hygroscopic Behavior

Figure 2(a–i) shows the hygroscopic response of each sulfate system as a function of RH. Droplet radial growth factor (rGF, blue markers, left axis) and refractive index at $\lambda = 589$ nm,

n(589 nm) (green markers, right axis), obtained from OT (triangle symbols) and EDB (circle symbols) measurements, show correlated but opposing trends: as RH increases, rGF increases due to water uptake while n(589 nm) decreases as the solution becomes more dilute. Bulk RI measurements (square symbols) at high RH closely match the single-droplet data, confirming calibration consistency under dilute conditions.

Upon decreasing RH from initially humid conditions ($\approx$ 90-95%), droplets of monovalent-cation sulfate salts, Li_2SO_4, Na_2SO_4, K_2SO_4, and $(NH_4)_2SO_4$, undergo smooth and continuous dehydration while remaining liquid, with efflorescence (crystallization of an aqueous droplet upon drying below a critical RH) occurring at approximately 46%, 56%, 68%, and 32% RH, respectively, as shown in Figure 2(a–d). OT and EDB data show very close agreement for both rGF and RI, with small systematic differences reflecting measurement technique and associated uncertainties rather than thermodynamic inconsistency. The monotonic increase in refractive index with decreasing RH indicates that these systems remain homogeneous aqueous solutions down to the point of efflorescence.

In contrast, divalent- and trivalent-cation sulfates exhibit more complex hygroscopic behavior. $MgSO_4$, $MnSO_4$, and $Al_2(SO_4)_3$ (Figure 2(e–g)) display pronounced inflection points at approximately 30–40% RH, consistent with partial solidification or the formation of highly viscous gel phases. Below these transitions, water loss becomes diffusion-limited: further compositional change with RH is strongly retarded and the optical properties vary only gradually at lower RH, consistent with kinetic limitations on water transport within semisolid matrices. Sulfates containing Mg^{2+} and Al^{3+} reach refractive indices of approximately 1.49 in the hydrated gel state, whereas Mn^{2+}-containing droplets exhibit higher values of approximately 1.53 in the gel phase. The gradual onset of gelation is consistent with increasingly strong multivalent-cation interactions and the progressive loss of complete solvation as RH decreases, which can promote network formation and gel-like phase transitions. This behavior parallels the humidity-dependent gel transitions reported for organic–inorganic aerosols, in which ion-mediated networks raise viscosity and suppress water transport,[34–37] and is in di-

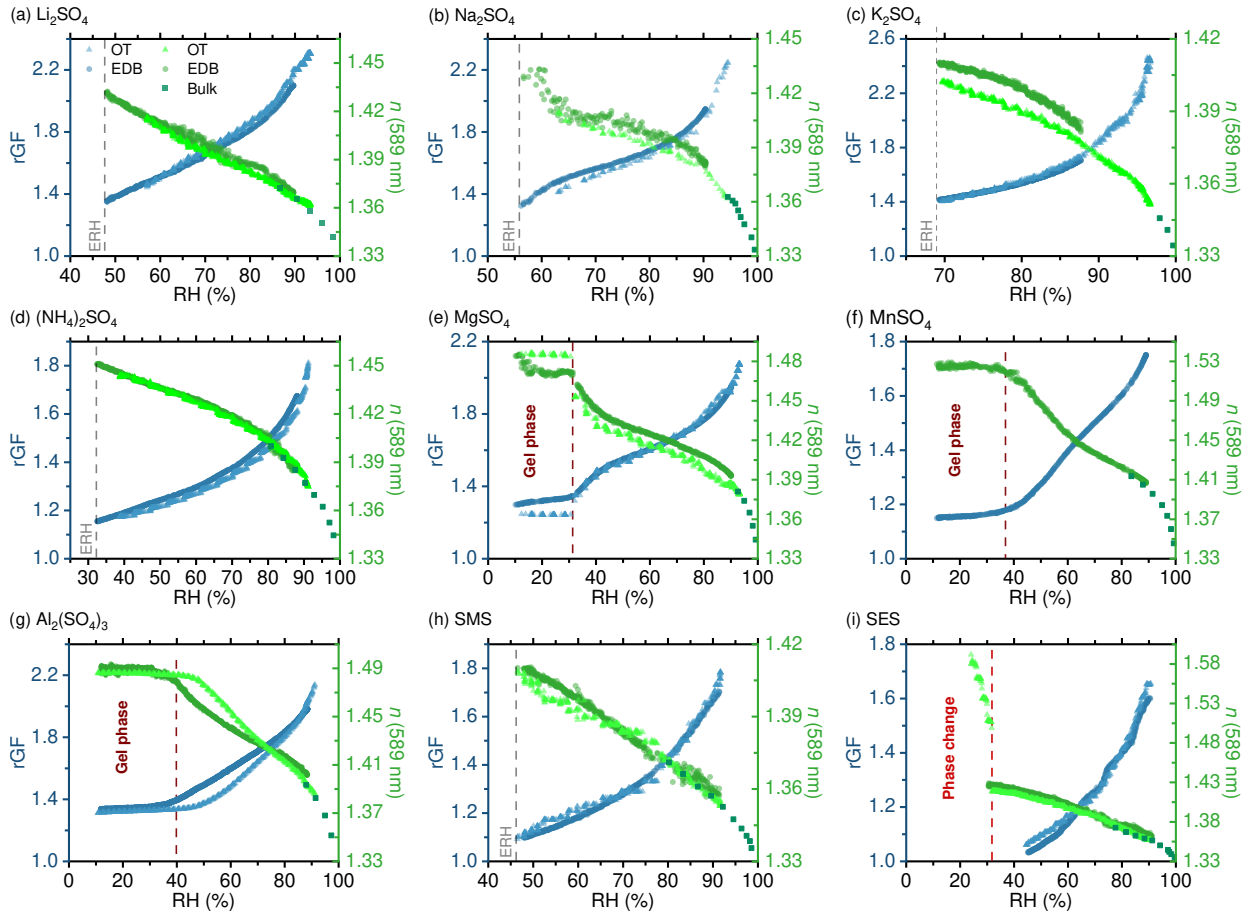

Figure 2: Hygroscopic growth behavior of levitated droplets composed of nine sulfate systems: (a) Li_2SO_4, (b) Na_2SO_4, (c) K_2SO_4, (d) $(NH_4)_2SO_4$, (e) $MgSO_4$, (f) $MnSO_4$, (g) $Al_2(SO_4)_3$, (h) sodium methyl sulfate (SMS), and (i) sodium ethyl sulfate (SES). Each panel presents the evolution of droplet radial growth factor (rGF, blue symbols, left axis) and refractive index at 589 nm (n(589 nm), green symbols, right axis) as a function of RH. Data are obtained using optical trapping (OT, triangle symbols) and electrodynamic balance (EDB, circle symbols) techniques, with bulk (square symbols) measurements shown for reference at high RH. The vertical dashed lines mark the relevant phase transition for each system: the efflorescence relative humidity (ERH) for the monovalent-cation salts (a–d) and SMS (h), the onset of the gel phase for the multivalent-cation salts $MgSO_4$, $MnSO_4$, and $Al_2(SO_4)_3$ (e–g), and the composition-dependent phase change for SES (i). Experimental uncertainties fall within the size of the symbols and represent an average of at least three independent measurements.

rect agreement with prior observations of contact-ion-pair networks and slow water transport in purely inorganic, supersaturated $MgSO_4$ droplets.[38–41] Due to absorption in the visible by $MnSO_4$, only hygroscopic measurements by the EDB method are provided (see Section 6 of the Supplementary Information for details).

Organosulfates (SMS and SES, Figure 2(h,i)) exhibit hygroscopic behavior intermediate between inorganic sulfates and surfactant-like organic species.[42] SMS shows smooth and reversible changes in size and refractive index over the full RH range and effloresces at RH ≈ 46%, whereas SES displays pronounced hysteresis and a composition-dependent phase transition below 30% RH. The elevated RI of SES at low RH, reaching values up to approximately 1.6 at 589 nm, is consistent with a transition to a distinct concentrated phase in this regime. As discussed in the following sections, the mass fraction of SES can exceed 0.9 at RH $< 40\%$, in contrast to the inorganic systems examined here.

3.2 BDE-Derived Thermodynamic Properties

Here, we discuss the extraction of thermodynamic properties of gel-forming sulfate aerosols using the BDE framework, and for the rest of the sulfates, discussions and results are provided in Section 7 of the Supplementary Information. The results of the BDE method from Section 2.2, summarized in Figure 3(a–c) for $MgSO_4$, $MnSO_4$, and $Al_2(SO_4)_3$, provide a unified framework linking droplet-scale measurements to bulk thermodynamic properties. For each gel-forming system, the BDE was applied to OT and EDB datasets to derive ρ, w, and concentration (C) as functions of RH. The retrieved parameters show strong internal consistency across techniques and reproduce bulk trends where data overlap, demonstrating that calibrated single-droplet measurements quantitatively recover equilibrium properties in supersaturated regimes. For comparison, the Aerosol Inorganic-Organic Mixture Functional Groups Activity Coefficients (AIOMFAC) thermodynamic model[43] predictions of w as a function of RH are also shown, where applicable. Measurements associated with bulk, AIOMFAC, OT, and EDB are indicated by red, orange, blue, and green symbols, respectively.

For these multivalent-cation systems, the physical properties do not freeze into an invariant state below the gelation threshold (RH ≈ 35 to 40%). Instead, the droplet enters a diffusion-limited regime in which water transport is strongly retarded but not entirely halted. Under deep dehydration toward RH ≈ 5%, the chemical-potential gradient drives a slow, con-

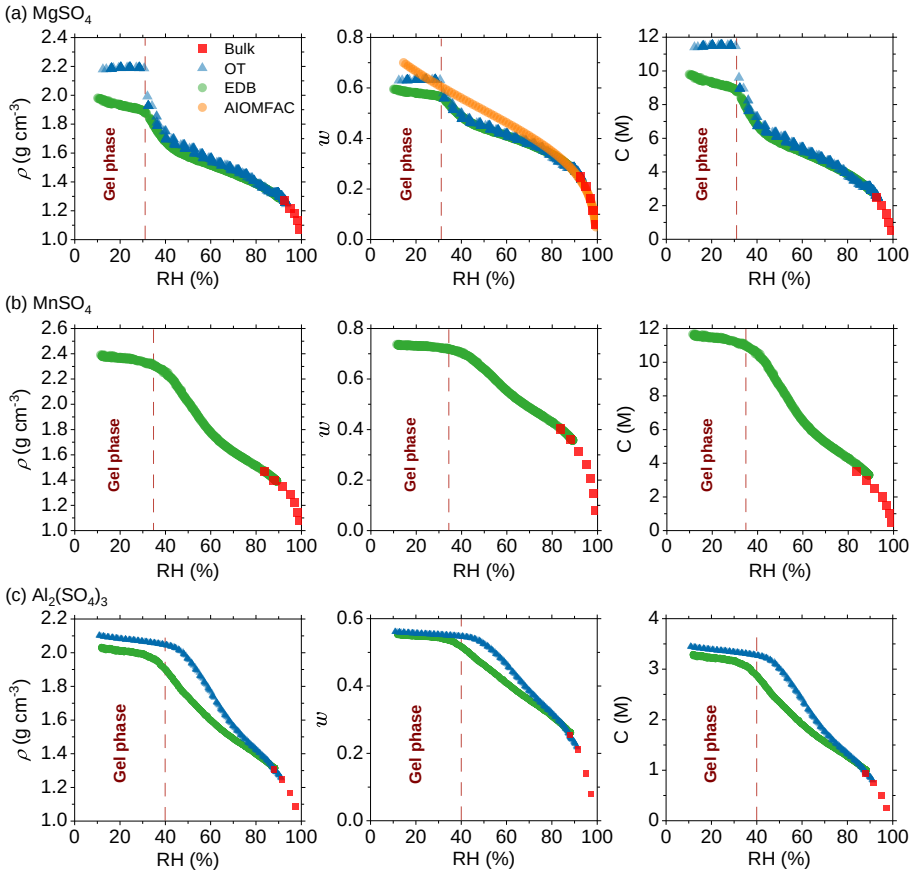

Figure 3: Thermodynamic properties of sulfate droplets derived from the BDE framework applied to OT and EDB measurements for (a) $MgSO_4$, (b) $MnSO_4$, and (c) $Al_2(SO_4)_3$. Panels show variations of density (ρ), solute mass fraction (w), and solute concentration in molarity (C) with RH. Red squares indicate bulk measurements, orange circles show the AIOMFAC predictions, blue triangles and green circles represent the OT and EDB measurements, respectively. The shaded gel region denotes a diffusion-limited regime in which slow, continuous water loss produces a gradual increase in density and refractive index, rather than a fully frozen or static phase state. Experimental uncertainties fall within the size of the symbols and represent an average of at least three independent measurements.

tinuous loss of residual water from the viscous network, producing a gradual densification (as seen in the slow rise in $MgSO_4$ density from ~2.2 to ~2.4 g cm^{-3} in Figure 3a). This decoupling between liquid and gel states indicates the onset of a semisolid matrix in which limited molecular mobility constrains additional densification. To probe water transport, OT measurements were conducted under hydration (increasing RH) while EDB experiments tracked dehydration (decreasing RH). This difference in RH trajectory and equilibration history helps explain the offset in the gel region between the OT and EDB measurements. As

shown in Figure 3, during hydration, gel-forming particles display only limited water uptake until the phase transition threshold, after which they rapidly absorb water and exhibit abrupt decreases in density, mass fraction, and concentration. During dehydration, water continues to leave the droplets after gel formation, but at markedly slower rates. $MgSO_4$, $MnSO_4$, and $Al_2(SO_4)_3$ reach maximum densities of approximately 2.2–2.4 g cm^{-3} in the gel phase, corresponding to mass fractions of roughly 0.6–0.7. Due to the larger molar mass of $Al_2(SO_4)_3$, its concentration in the gel regime is substantially lower (about 3.4 M) than those of $MgSO_4$ and $MnSO_4$, which exceed 11 M.

3.3 Density–Mass Fraction–RI Relationships

Figure 4(a–c) shows the relationship between ρ and w and wavelength-dependent RI for the investigated gel-forming sulfate systems, and the same discussion for the rest of the systems is provided in Section 8 of the Supplementary Information. These plots combine bulk measurements, reference literature values,[31,32,44] and densities and mass fractions retrieved from levitated droplets using the BDE framework. Two quadratic parameterizations are applied: an orange curve constrained solely by bulk and literature data, and a blue curve that additionally incorporates averaged BDE-derived droplet densities from OT and EDB measurements. Inclusion of the droplet-derived data extends the fit constraints to high solute fractions, where parameterizations based only on bulk data tend to underestimate density for these systems. These systems persist in highly concentrated, gel-like states and reach substantially higher densities than the monovalent-cation sulfate salts, exceeding 2.0 g cm^{-3}, 2.4 g cm^{-3}, and 2.2 g cm^{-3} for Mg^{2+}-, Mn^{2+}-, and Al^{3+}-containing sulfate systems, respectively.

The middle panels in Figure 4 show the variation of the real part of the refractive index (n) at 589 nm with solute mass fraction (w), and the effective oscillator model provides linear fits to the OT and EDB datasets separately and captures the overall concentration dependence. In all systems, n increases monotonically with w, reflecting the higher refractive index of increasingly concentrated solutions. These systems show noticeably steep increases in n with

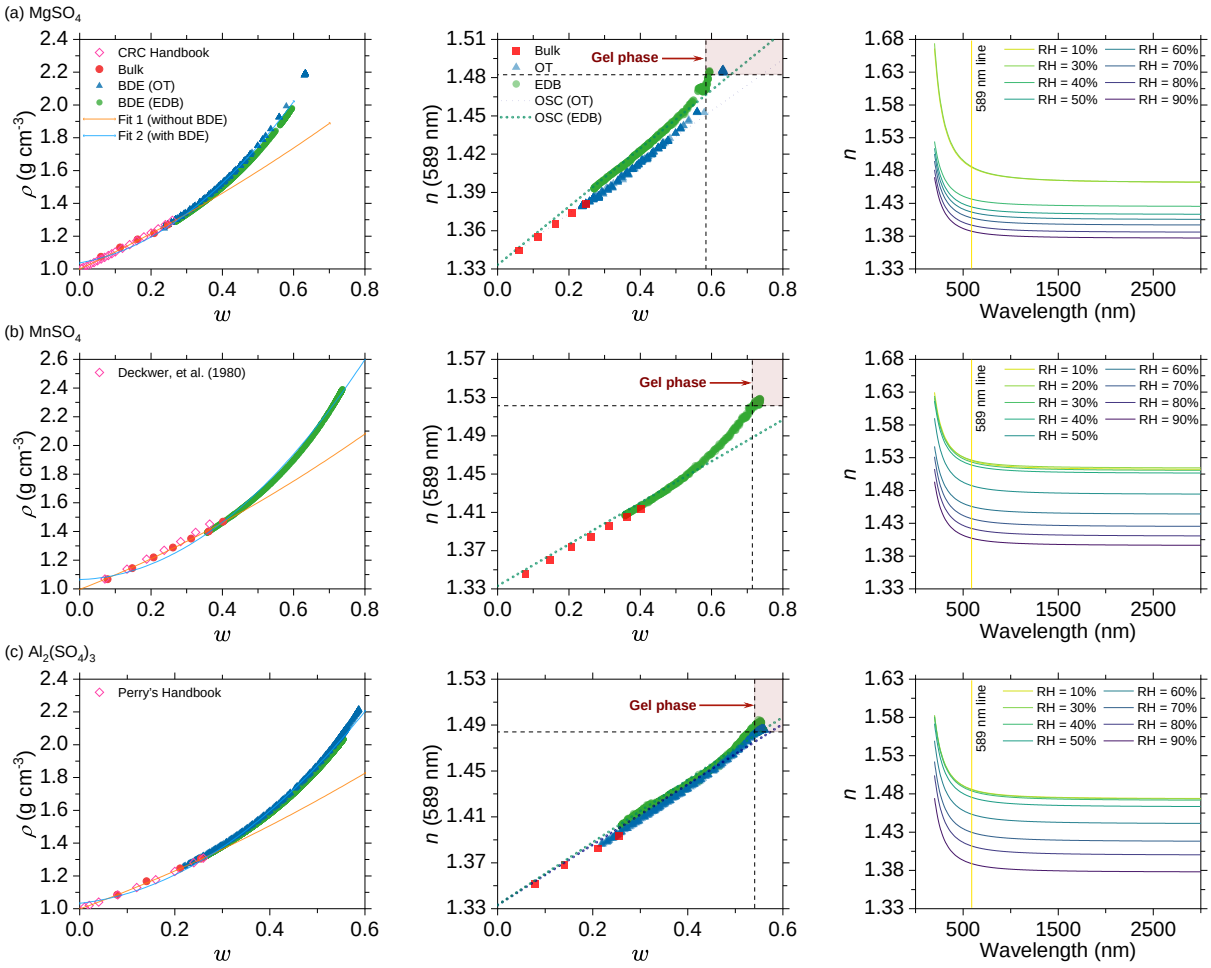

Figure 4: Relations between density (ρ), solute mass fraction (w), and refractive index for (a) $MgSO_4$, (b) $MnSO_4$, and (c) $Al_2(SO_4)_3$. Pink diamonds, Red squares, blue triangles, and green circles indicate literature values, bulk measurements, OT, and EDB measurements, respectively. Left panel shows ρ as a function of w and orange and blue curves illustrate the bulk and bulk plus droplet fits. The middle panel shows $n(589\text{ nm})$ as a function of w, and the effective oscillator model provides the fit to this data. The right panel provides the wavelength dependence of RI at different RH values. The shaded gel region denotes a diffusion-limited regime in which slow, continuous water loss produces a gradual increase in density and refractive index, rather than a fully frozen or static phase state.

w at high concentrations. Nonlinear behavior emerges at high w, coincident with the onset of gel formation. This behavior is driven by strong multivalent-cation interactions, ion pairing, and localized alterations to the hydration structure, which modify the molecular packing and electronic polarizability as the rigid network forms. For $MgSO_4$, n increases to ~ 1.49 before approaching a plateau. $Al_2(SO_4)_3$ reaches $n \approx 1.49$, while $MnSO_4$ reaches $n \approx 1.53$. In this

regime, the model captures most trends, but small deviations arise, especially for $MnSO_4$. Beyond the identified transition, water loss becomes diffusion-limited and the mass fraction changes only gradually, so the refractive index likewise varies only weakly and remains near its maximum value. The oscillator model fitting parameters are given in Section 9 of the Supplementary Information.

The right panel in Figure 4 represents the spectral dispersion of the real refractive index at different RH values using the effective oscillator model fitting parameters provided in Section S9 of the Supplementary Information. These multivalent-cation gel-forming sulfates display steep dispersion slopes and higher refractive indices under dry conditions, consistent with stronger electrostatic interactions and more structured hydration environments. $MgSO_4$ in the gel regime reaches n values approaching ~ 1.67 at the shortest wavelengths, whereas $MnSO_4$ exhibits the highest n at longer wavelengths, reaching approximately 1.53. These behaviors reflect the combined influences of charge density, hydration structure, and phase state on the determination of the refractive index.

Overall, these results show that common quadratic models underestimate density at high concentrations and that entry into the gel regime causes the refractive index to vary nonlinearly with concentration. More broadly, the BDE-derived thermodynamic properties provide a framework for linking hydration state to optical behavior, including the wavelength dependence of the refractive index. These system-specific dispersion characteristics are important for accurately representing sulfate aerosols in radiative transfer and climate models and may also inform assessments of their suitability for geoengineering applications, particularly in cases where water transport is strongly suppressed.

4 Environmental Implications

4.1 Relevance to Tropospheric Sulfate Aerosol and Model Constraints

The measurements reported here provide useful constraints for tropospheric aerosol models because ambient sulfate-containing particles are rarely pure H_2SO_4–H_2O solutions and often contain a diverse set of inorganic ions derived from sea spray, mineral dust processing, and anthropogenic emissions.[25,45,46] While hygroscopic growth and refractive index parameterizations for several inorganic salts and sulfate solutions have been reported previously,[30,47] Figures 2–3 demonstrate that sulfate composition can strongly govern hygroscopic growth and phase behavior across atmospherically relevant RH, including regimes where equilibrium assumptions may break down. The monovalent-cation sulfate salts show comparatively smooth hygroscopic growth (Fig. 2a–d), whereas the multivalent-cation systems $MgSO_4$, $Al_2(SO_4)_3$, and $MnSO_4$ exhibit pronounced inflection points and hysteresis consistent with transitions into highly viscous, gel-like states (Fig. 2e–g). Such behavior is not represented in many large-scale models that assume rapid equilibration to a fully liquid state and represent water uptake using a single, smoothly varying relationship.[43,46] In the troposphere, these phase-state transitions may be particularly relevant for internally mixed particles influenced by sea-salt cations (e.g., Mg^{2+}) and for aerosols that experience repeated drying–rehydration cycles, where kinetic limitations and hysteresis can affect particle size evolution, optical properties, and cloud activation behavior. We also observe that SES forms a highly viscous state under dry conditions, whereas SMS does not, suggesting that the tendency for short-chain organosulfates to transition into highly viscous or semisolid phases may be compound-specific and not straightforward to generalize from carbon number alone.

The BDE-derived thermodynamic and optical datasets further constrain key state variables used in tropospheric aerosol modules. Figure 3 provides internally consistent relationships between density, mass fraction, and concentration with water activity, enabling improved conversion between aerosol mass, volume, and water content under metastable con-

ditions. These quantities directly influence simulated aerosol optical depth and hygroscopic growth factors used in aerosol–radiation interactions, as well as the sensitivity of activation to RH and supersaturation in aerosol–cloud interactions. In parallel, Fig. 4 illustrates that first, simple quadratic parameterizations of the metastable regime can produce biased estimates, systematically underpredicting solution densities (left panel in Fig. 4), and second, the refractive index varies substantially with composition and concentration, and that wavelength-dependent refractive indices are required to capture shortwave optical behavior. This is most pronounced for the gel-forming sulfates at high mass fractions, where $n(w, \lambda)$ increases strongly (middle and the right panels in Fig. 4), implying that adopting a fixed, composition-independent refractive index for "sulfate" may lead to biases in simulated scattering efficiencies and retrieval forward models. Together, these results provide a pathway for incorporating composition- and RH-dependent density, water activity, and refractive index into tropospheric aerosol models, reducing reliance on simplified assumptions for sulfate optical properties and hygroscopic growth.

In realistic atmospheric aerosols, mixtures of monovalent and multivalent cations are common. Our framework can be extended to such systems using composition-weighted thermodynamic parameters, though synergistic gel formation may occur at distinct RH values for each component. Models that neglect multivalent cations and assume fully aqueous sulfate may therefore overestimate cloud activation efficiency and heterogeneous reaction rates.

To connect these experimental parameters to large-scale frameworks, we suggest several coupling pathways targeting specific calculations in current chemical transport models (CTMs) such as GEOS-Chem[48] and WRF-Chem.[49] First, equilibrium thermodynamic submodules such as ISORROPIA-II[50] and MOSAIC[51] treat crustal and marine cations (e.g., Mg^{2+}, Ca^{2+}) by relaxing the condensed phase to internal thermodynamic equilibrium and do not represent the slow intraparticle diffusion that accompanies gel formation. The density, water activity, and composition relationships reported here can serve as inputs to kinetically resolved water-uptake schemes for these systems, replacing the assumption of instantaneous

equilibration once a gel phase forms. Second, aerosol optical properties in these models are computed from Mie or lookup tables that assign each species a fixed, composition-independent dry refractive index and an RH-dependent growth factor, and the resulting aerosol optical depth (AOD), single-scattering albedo, and asymmetry parameter are then passed to the radiation solver (e.g., RRTMG).[52] Assigning sulfate a single refractive index misses the elevated values of the gel phase ($\sim$1.49 to 1.53) at low RH and underestimates the mass extinction efficiency (MEE) and column AOD; the RH-dependent refractive index from our effective oscillator parameters provides a direct correction under dry conditions. Third, for cloud condensation nuclei (CCN) activation parameterizations such as that of Abdul-Razzak and Ghan,[53] the high viscosity of the gel state can delay water uptake in particles that enter an updraft from a low-RH state, so equilibrium Köhler treatments may overestimate the activated fraction for these systems.

These considerations become more complex for internally mixed particles, such as anthropogenic sulfate coatings on marine sea salt (a source of Mg^{2+}) or on mineral dust rich in Al^{3+}, Mn^{2+}, and Ca^{2+}. In such systems, linear, volume-weighted mixing rules are unlikely to hold, because the co-existence of multivalent cations and sulfate can promote interionic cross-linking and network formation even when the multivalent species are a minority of the mass. During dehydration, spatial gradients in water loss could promote phase separation, with a more viscous outer region surrounding a more dilute core; such a configuration could act as a kinetic barrier to water transport and could lower the heterogeneous uptake coefficients (γ) of trace gases such as N_2O_5, O_3, and halogens.[54,55] We note that the present measurements do not resolve particle morphology directly, so this internal-mixture behavior is presented as a hypothesis that motivates targeted measurements and core-shell kinetic modeling rather than as an established result.

4.2 Gel-Forming Multivalent Sulfates as Candidates for Stratospheric Aerosol Injection (SAI)

A key outcome of this work is that sulfate aerosols containing multivalent cations ($MgSO_4$, $Al_2(SO_4)_3$, and $MnSO_4$) exhibit a distinct phase-state transition that may be advantageous for SAI. Our single-particle measurements and BDE-derived thermodynamics show that these systems form highly viscous, gel-like phases below RH $\approx$ 35–40%, characterized by limited water transport and weak sensitivity of particle properties to further drying (Fig. 3). In particular, once droplets enter the gel regime, their density, refractive index, and radial growth factor change only modestly with decreasing RH (during hydration they display only limited water uptake until the transition threshold is crossed, after which rapid rehydration occurs). This "humidity-buffered" behavior contrasts with more typical inorganic sulfates that undergo strong hygroscopic growth at high RH and/or efflorescence-driven discontinuities. In the context of SAI, the weak RH dependence of size and optical properties (high RI) in the low-RH gel regime implies that gel-forming sulfates may better preserve an optimized size distribution (and thus shortwave forcing efficiency) against variations in ambient humidity and microphysical history.

To quantify the shortwave radiative implications of these gel-forming sulfates, we computed shortwave forcing efficiencies by combining Mie theory optical properties with 1D radiative transfer calculations. For each composition and each effective radius, r_{eff}, and geometric standard deviation, σ_g, pair, we defined a lognormal particle size distribution and computed the extinction efficiency Q_{ext}, single-scattering albedo ω, and asymmetry parameter g as a function of wavelength using Mie theory for homogeneous spheres.[56,57] Distribution-mean optical properties were obtained by averaging over particle radius using geometric cross-section weighting for extinction, with scattering-weighted averaging used for ω and g (consistent with bulk radiative transfer requirements). Radiative forcing efficiencies were then obtained by passing these distribution-mean optical properties to 1D shortwave radiative transfer calculations (libRadtran/uvspec[58,59] with DISORT[60]), as described in the Supporting Information.

Figure 5 shows calculated shortwave forcing efficiencies for gel phase $MgSO_4$ (a–c), $MnSO_4$ (d–f), and $Al_2(SO_4)_3$ (g–i), with optical properties derived from the measured wavelength-dependent refractive indices at RH $< 30\,\%$, which is representative of the generally dry lower stratosphere.[61] For reference, calculations for sulfate aerosol were performed using optical properties from Dykema et al.[62]. These results are shown in panels (j–l). Overall, the gel-forming sulfates exhibit forcing efficiencies comparable in magnitude to conventional sulfate aerosols and the presence of multivalent cations does not reduce radiative forcing. Instead, a modest amplification is observed in both forcing magnitude and optimal particle size, with enhancements of $\approx 5\%$. Radiative forcing calculations here neglect absorption. This approximation is justified because, for particles in the size range considered, shortwave forcing is insensitive to weak visible absorption with $k < 10^{-2}$.[63] Of the four species, $MnSO_4$ has the strongest visible absorption, but even at high concentrations its imaginary refractive index remains well below this threshold, with k on the order of 10^{-6} (see Fig. S4).

Beyond microphysics, candidate materials for SAI must also be evaluated in terms of scalability and environmental side effects. A sustained SAI deployment capable of producing climate-relevant forcing would require Tg-scale atmospheric burdens and continuous resupply, implying that the choice of injected material is necessarily coupled to industrial production capacity and supply-chain constraints. Recent assessments highlight both the feasibility of scaling SAI delivery technologies and the substantial uncertainties associated with stratospheric aerosol evolution and impacts.[64] In this context, Hack et al.[65] emphasize that raw-material production capacity and market responsiveness can materially constrain candidate selection: for widely produced precursors such as alumina and mined sulfur (an SO_2 source), the material demand associated with representative multi-decade strategies can remain at the sub-percent level of current global production, yet these markets tend to exhibit near-inelastic demand, implying that more aggressive forcing targets or prolonged deployment could still place nontrivial pressure on supply chains.[65] From this perspective, $MgSO_4$ and $Al_2(SO_4)_3$ benefit from comparatively mature and high-volume precursor supply chains: global primary

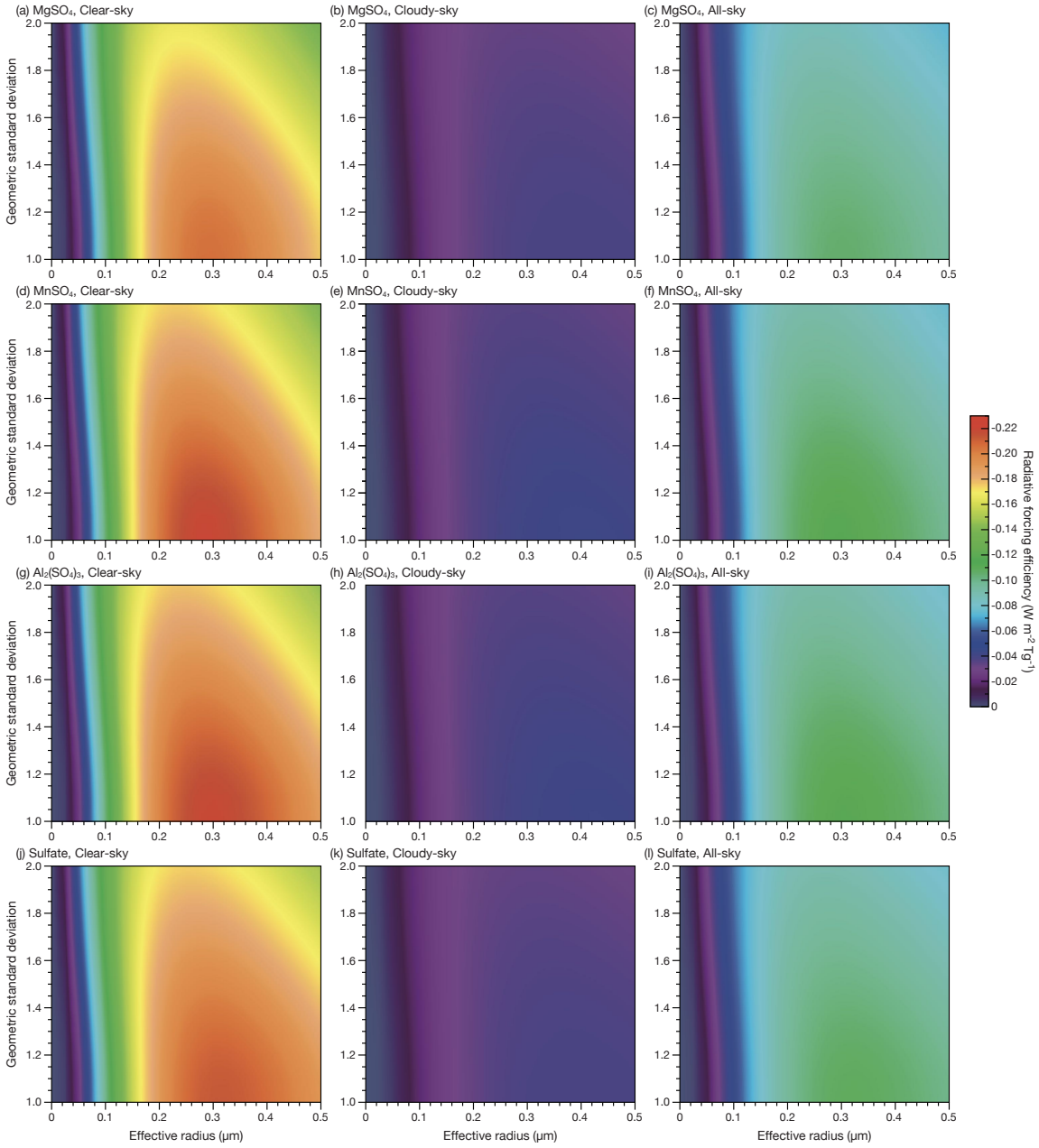

Figure 5: Shortwave radiative forcing efficiency ($\mathrm{W\,m^{-2}\,Tg^{-1}}$) as a function of effective radius and geometric standard deviation for stratospheric aerosol injection of (a–c) $MgSO_4$, (d–f) $MnSO_4$, (g–i) $Al_2(SO_4)_3$, and (j–l) sulfate. Results are shown for clear-sky (left column; cloud-free atmosphere), cloudy-sky (center column; overcast conditions), and all-sky (right column) conditions. All-sky forcing is computed using the Independent Column Approximation (ICA) with a cloud fraction $A_c = 0.6$. For panels (j–l), sulfate aerosol optical properties are taken from Dykema et al.[62] Calculations assume a 1 Tg global aerosol burden uniformly distributed between 18–23 km altitude. More negative values indicate stronger cooling (greater reflected shortwave radiation at the top of the atmosphere). The colorbar applies to all panels.

magnesium metal production is on the order of ∼1 Mt yr^{-1}, while primary aluminum production exceeds 70 Mt yr^{-1} with well-established worldwide refining infrastructure.[66,67] In contrast, for $MnSO_4$ in particular, demand for high-purity manganese sulfate is rising due to its role as a precursor for electric-vehicle battery cathode materials, potentially creating competition between SAI-scale deployment and critical clean-energy supply chains.[68,69] More broadly, geographic concentration of upstream production and trade flows in a small number of regions can increase vulnerability to disruptions, as highlighted in recent analyses of global magnesium trade network structure and evolution.[70]

Finally, chemical reactivity remains a central concern for any stratospheric aerosol intervention. It is well established from volcanic analogues and chemistry–climate modeling that increases in aerosol surface area enhance heterogeneous reactions that activate halogens and promote catalytic ozone destruction in the stratosphere, in part by increasing the surface available for reactions involving adsorbed water.[71–73] However, if multivalent sulfates such as $MgSO_4$, $Al_2(SO_4)_3$, and $MnSO_4$ form gel-like phases, diffusion-limited transport within the particles may partially suppress these reactions relative to those in fully aqueous sulfate aerosols. For example, recent laboratory measurements on gel-state aerosol analogs show that heterogeneous oxidation can become transport-limited below ∼40% RH, leading to strongly suppressed effective reaction rates as particles transition into gel phases.[74] Consistent with this picture, temperature- and RH-dependent viscosity measurements for sucrose–H_2O aerosol proxies showed that the N_2O_5 uptake coefficient decreases by about 1–2 orders of magnitude as particles become semisolid and diffusion-limited and, in the absence of surface hydrolysis, can fall to 10^{-5}–10^{-6} at viscosities above $\sim 10^9$ Pa s.[75] In addition, heterogeneous chemistry on fully liquid H_2SO_4–H_2O aerosols is expected to be surface accommodation-limited,[55] whereas diffusion and water-availability constraints in $MgSO_4$, $Al_2(SO_4)_3$, and $MnSO_4$ gels could shift uptake toward transport-limited behavior and thereby reduce effective heterogeneous reactivity. Quantifying these effects will require laboratory constraints on heterogeneous uptake coefficients and particle-phase transport in the gel regime, together

with chemistry–climate simulations that explicitly represent phase state. Restricting attention to physical and chemical considerations (and not cost or deployment logistics), the broadly similar shortwave forcing efficiencies in Fig. 5 imply that, if longwave absorption is also comparable, differences in heterogeneous reactivity and associated ozone impacts may ultimately be the key factor differentiating their suitability for SAI.

Acknowledgement

All authors acknowledge financial support from the Simons Foundation (SFI-MPS-SRM-00005211).

Data Availability. The measured wavelength-dependent refractive indices used to generate Figure 5 are provided in Dataset S1 (`Sulfate_Measurements.xlsx`) and as effective-oscillator parameters in Supplementary Table S1. The radiative-transfer configuration is described in Supplementary Section S10. All calculations used the publicly available libRadtran/uvspec package and its bundled Mie tool.

Supporting Information Available

Additional experimental details, Supplementary Sections S1–S10, Supplementary Figures S1–S7, and Supplementary Tables S1–S2 (PDF). An accompanying Excel workbook (Dataset S1: `Sulfate_Measurements.xlsx`) containing all reported measurements.

References

(1) Robock, A. Volcanic eruptions and climate. *Rev. Geophys.* **2000**, *38*, 191–219, DOI: 10.1029/1998RG000054.

(2) Stenchikov, G. L.; Kirchner, I.; Robock, A.; Graf, H.-F.; Antuna, J. C.; Grainger, R. G.; Lambert, A.; Thomason, L. Radiative forcing from the 1991 Mount Pinatubo volcanic eruption. *J. Geophys. Res. Atmos.* **1998**, *103*, 13837–13857, DOI: 10.1029/98JD00693.

(3) Charlson, R. J.; Schwartz, S. E.; Hales, J. M.; Cess, R. D.; Coakley Jr, J. A.; Hansen, J. E.; Hofmann, D. J. Climate forcing by anthropogenic aerosols. *Science* **1992**, *255*, 423–430, DOI: 10.1126/science.255.5043.423.

(4) Seinfeld, J. H.; Pandis, S. N. *Atmospheric chemistry and physics: from air pollution to climate change*; John Wiley & Sons, 2016.

(5) Intergovernmental Panel on Climate Change *Climate Change 2013: The Physical Science Basis*; 2013.

(6) Cziczo, D. J.; Froyd, K. D.; Gallavardin, S. J.; Moehler, O.; Benz, S.; Saathoff, H.; Murphy, D. M. Deactivation of ice nuclei due to atmospherically relevant surface coatings. *Environ. Res. Lett.* **2009**, *4*, 044013, DOI: 10.1088/1748-9326/4/4/044013.

(7) Iinuma, Y.; Böge, O.; Gnauk, T.; Herrmann, H. Aerosol-chamber study of the α-pinene/O3 reaction: influence of particle acidity on aerosol yields and products. *Atmos. Environ.* **2004**, *38*, 761–773, DOI: 10.1016/j.atmosenv.2003.10.015.

(8) Twomey, S. The influence of pollution on the shortwave albedo of clouds. *J. Atmos. Sci.* **1977**, *34*, 1149–1152, DOI: 10.1175/1520-0469(1977)034<1149:TIOPOT>2.0.CO;2.

(9) Boucher, O.; Lohmann, U. The sulfate-CCN-cloud albedo effect. *Tellus B: Chem. Phys. Meteorol.* **1995**, *47*, 281–300, DOI: 10.3402/tellusb.v47i3.16048.

(10) Haywood, J.; Boucher, O. Estimates of the direct and indirect radiative forcing due to tropospheric aerosols: A review. *Rev. Geophys.* **2000**, *38*, 513–543, DOI: 10.1029/1999RG000078.

(11) Ghan, S. J.; Easter, R. C.; Chapman, E. G.; Abdul-Razzak, H.; Zhang, Y.; Leung, L. R.; Laulainen, N. S.; Saylor, R. D.; Zaveri, R. A. A physically based estimate of radiative forcing by anthropogenic sulfate aerosol. *J. Geophys. Res. Atmos.* **2001**, *106*, 5279–5293, DOI: 10.1029/2000JD900503.

(12) Feichter, J.; Kjellström, E.; Rodhe, H.; Dentener, F.; Lelieveld, J.; Roelofs, G.-J. Simulation of the tropospheric sulfur cycle in a global climate model. *Atmos. Environ.* **1996**, *30*, 1693–1707, DOI: 10.1016/1352-2310(95)00394-0.

(13) Brooks, S. D.; Thornton, D. C. O. Marine aerosols and clouds. *Annu. Rev. Mar. Sci.* **2018**, *10*, 289–313, DOI: 10.1146/annurev-marine-121916-063148.

(14) O'Dowd, C. D.; Smith, M. H.; Consterdine, I. E.; Lowe, J. A. Marine aerosol, sea-salt, and the marine sulphur cycle: A short review. *Atmos. Environ.* **1997**, *31*, 73–80, DOI: 10.1016/S1352-2310(96)00106-9.

(15) Finlayson-Pitts, B. J.; Pitts Jr, J. N. *Chemistry of the upper and lower atmosphere: theory, experiments, and applications*; Elsevier, 1999.

(16) Jacob, D. J. *Introduction to Atmospheric Chemistry*; Princeton University Press, 1999.

(17) Andreae, M. O.; Crutzen, P. J. Atmospheric aerosols: Biogeochemical sources and role in atmospheric chemistry. *Science* **1997**, *276*, 1052–1058, DOI: 10.1126/science.276.5315.1052.

(18) Wang, Y.; Hu, M.; Wang, Y.-C.; Li, X.; Fang, X.; Tang, R.; Lu, S.; Wu, Y.; Guo, S.; Wu, Z.; others Comparative study of particulate organosulfates in contrasting atmospheric environments: Field evidence for the significant influence of an-

559 thropogenic sulfate and NO_x. *Environ. Sci. Technol. Lett.* **2020**, *7*, 787–794, DOI:
560 10.1021/acs.estlett.0c00550.

561 (19) Ervens, B. Modeling the processing of aerosol and trace gases in clouds and fogs. *Chem.*
562 *Rev.* **2015**, *115*, 4157–4198, DOI: 10.1021/cr5005887.

563 (20) Pöhlker, M. L.; Pöhlker, C.; Quaas, J.; Mülmenstädt, J.; Pozzer, A.; Andreae, M. O.;
564 Artaxo, P.; Block, K.; Coe, H.; Ervens, B.; others Global organic and inorganic aerosol
565 hygroscopicity and its effect on radiative forcing. *Nat. Commun.* **2023**, *14*, 6139, DOI:
566 10.1038/s41467-023-41695-8.

567 (21) Twomey, S. Aerosols, clouds and radiation. *Atmos. Environ., Part A* **1991**, *25*, 2435–
568 2442, DOI: 10.1016/0960-1686(91)90159-5.

569 (22) Rosenfeld, D.; Andreae, M. O.; Asmi, A.; Chin, M.; de Leeuw, G.; Donovan, D. P.;
570 Kahn, R.; Kinne, S.; Kivekäs, N.; Kulmala, M.; others Global observations of
571 aerosol-cloud-precipitation-climate interactions. *Rev. Geophys.* **2014**, *52*, 750–808, DOI:
572 10.1002/2013RG000441.

573 (23) Boucher, O.; Randall, D.; Artaxo, P.; Bretherton, C.; Feingold, G.; Forster, P.; Ker-
574 minen, V.-M.; Kondo, Y.; Liao, H.; Lohmann, U.; others *Climate change 2013: The*
575 *physical science basis. Contribution of working group I to the fifth assessment report of*
576 *the intergovernmental panel on climate change*; Cambridge University Press, 2013; pp
577 571–657.

578 (24) Yang, Y.; Wang, H.; Smith, S. J.; Easter, R.; Ma, P.-L.; Qian, Y.; Yu, H.;
579 Li, C.; Rasch, P. J. Global source attribution of sulfate concentration and direct
580 and indirect radiative forcing. *Atmos. Chem. Phys.* **2017**, *17*, 8903–8922, DOI:
581 10.5194/acp-17-8903-2017.

582 (25) Bertram, T. H.; Cochran, R. E.; Grassian, V. H.; Stone, E. A. Sea spray aerosol
583 chemical composition: elemental and molecular mimics for laboratory studies of het-

erogeneous and multiphase reactions. *Chem. Soc. Rev.* **2018**, *47*, 2374–2400, DOI: 10.1039/C7CS00008A.

(26) Mahowald, N. M.; Hamilton, D. S.; Mackey, K. R. M.; Moore, J. K.; Baker, A. R.; Scanza, R. A.; Zhang, Y. Aerosol trace metal leaching and impacts on marine microorganisms. *Nat. Commun.* **2018**, *9*, 2614, DOI: 10.1038/s41467-018-04970-7.

(27) Zhang, Y.; Mahowald, N.; Scanza, R. A.; Journet, E.; Desboeufs, K.; Albani, S.; Kok, J. F.; Zhuang, G.; Chen, Y.; Cohen, D. D.; others Modeling the global emission, transport and deposition of trace elements associated with mineral dust. *Biogeosciences* **2015**, *12*, 5771–5792, DOI: 10.5194/bg-12-5771-2015.

(28) Wang, W.; Liu, M.; Wang, T.; Song, Y.; Zhou, L.; Cao, J.; Hu, J.; Tang, G.; Chen, Z.; Li, Z.; others Sulfate formation is dominated by manganese-catalyzed oxidation of SO2 on aerosol surfaces during haze events. *Nat. Commun.* **2021**, *12*, 1993, DOI: 10.1038/s41467-021-22091-6.

(29) Zhang, T.; Chen, Y.; Zhang, H.; Liu, L.; Huang, C.; Fang, Z.; Zhang, Y.; Wang, F.; Luo, L.; Zhang, G.; others Atmospheric chemical processing dictates aerosol aluminum solubility: insights from field measurement at two locations in Northern China. *Atmos. Chem. Phys.* **2025**, *25*, 17091–17106, DOI: 10.5194/acp-25-17091-2025.

(30) Tang, I. N.; Munkelwitz, H. R. Water activities, densities, and refractive indices of aqueous sulfates and sodium nitrate droplets of atmospheric importance. *J. Geophys. Res. Atmos.* **1994**, *99*, 18801–18808, DOI: 10.1029/94JD01345.

(31) Rumble, J. R., Ed. *CRC Handbook of Chemistry and Physics*, 106th ed.; CRC Press: Boca Raton, FL, 2025.

(32) Deckwer, W. D. Density, viscosity, vapor pressure, and hydrogen solubility of aqueous manganese (II) sulfate solutions. *J. Chem. Eng. Data* **1980**, *25*, 75–76, DOI: 10.1021/je60084a022.

(33) Bain, A.; Chan, M. N.; Bzdek, B. R. Physical properties of short chain aqueous organosulfate aerosol. *Environ. Sci.: Atmos.* **2023**, *3*, 1365–1373, DOI: 10.1039/d3ea00088e.

(34) Richards, D. S.; Trobaugh, K. L.; Hajek-Herrera, J.; Price, C. L.; Sheldon, C. S.; Davies, J. F.; Davis, R. D. Ion-Molecule Interactions Enable Unexpected Phase Transitions in Organic-Inorganic Aerosol. *Sci. Adv.* **2020**, *6*, eabb5643, DOI: 10.1126/sciadv.abb5643.

(35) Richards, D. S.; Trobaugh, K. L.; Hajek-Herrera, J.; Davis, R. D. Dual-Balance Electrodynamic Trap as a Microanalytical Tool for Identifying Gel Transitions and Viscous Properties of Levitated Aerosol Particles. *Anal. Chem.* **2020**, *92*, 3086–3094, DOI: 10.1021/acs.analchem.9b04487.

(36) Sheldon, C. S.; Salazar, J.; Palacios Diaz, T.; Morton, K.; Davis, R. D.; Davies, J. F. Correlating the Viscosity and Rate of Water Diffusion in Semisolid Gel-Forming Aerosol Particles. *ACS Earth Space Chem.* **2023**, *7*, 2311–2320, DOI: 10.1021/acsearthspacechem.3c00241.

(37) Dong, F.; Huang, Q.; Pang, S.; Zhang, Y.-H. Hydrogel Network Formation Triggers Atypical Hygroscopic Behavior in Atmospheric Aerosols. *Sci. Total Environ.* **2024**, *956*, 177298, DOI: 10.1016/j.scitotenv.2024.177298.

(38) Zhang, Y.-H.; Chan, C. K. Study of Contact Ion Pairs of Supersaturated Magnesium Sulfate Solutions Using Raman Scattering of Levitated Single Droplets. *J. Phys. Chem. A* **2000**, *104*, 9191–9196, DOI: 10.1021/jp0013659.

(39) Wang, F.; Zhang, Y.-H.; Li, S.-H.; Wang, L.-Y.; Zhao, L.-J. A Strategy for Single Supersaturated Droplet Analysis: Confocal Raman Investigations on the Complicated Hygroscopic Properties of Individual $MgSO_4$ Droplets on the Quartz Substrate. *Anal. Chem.* **2005**, *77*, 7148–7155, DOI: 10.1021/ac050938g.

(40) Zhao, L.-J.; Zhang, Y.-H.; Hu, Y.-A.; Ding, F. Observations of Supersaturated $MgSO_4$ and $NaClO_4$ Aerosols by FTIR/ATR Spectroscopy. *Atmos. Res.* **2007**, *83*, 10–18, DOI: 10.1016/j.atmosres.2006.02.003.

(41) Cai, C.; Tan, S.; Chen, H.; Ma, J.; Wang, Y.; Reid, J. P.; Zhang, Y.-H. Slow Water Transport in $MgSO_4$ Aerosol Droplets at Gel-Forming Relative Humidities. *Phys. Chem. Chem. Phys.* **2015**, *17*, 29753–29763, DOI: 10.1039/C5CP05181A.

(42) Shahabadi, V.; Lefort, C.; Law, H. T.; Chan, M. N.; Preston, T. C. Surface tension and hygroscopicity analysis of aerosols containing organosulfate surfactants. *Atmos. Chem. Phys.* **2025**, *25*, 14301–14313, DOI: 10.5194/acp-25-14301-2025.

(43) Zuend, A.; Marcolli, C.; Luo, B. P.; Peter, T. A thermodynamic model of mixed organic–inorganic aerosols to predict activity coefficients. *Atmos. Chem. Phys.* **2008**, *8*, 4559–4593, DOI: 10.5194/acp-8-4559-2008.

(44) Perry, J. H. Chemical engineers' handbook. 1950.

(45) Jayarathne, T.; Sultana, C. M.; Lee, C.; Malfatti, F.; Cox, J. L.; Pendergraft, M. A.; Moore, K. A.; Azam, F.; Tivanski, A. V.; Cappa, C. D.; Bertram, T. H.; Grassian, V. H.; Prather, K. A.; Stone, E. A. Enrichment of Saccharides and Divalent Cations in Sea Spray Aerosol During Two Phytoplankton Blooms. *Environ. Sci. Technol.* **2016**, *50*, 11511–11520, DOI: 10.1021/acs.est.6b02988.

(46) Wexler, A. S.; Clegg, S. L. Atmospheric aerosol models for systems including the ions H^+, NH_4^+, Na^+, SO_4^{2-}, NO_3^-, Cl^-, Br^-, and H_2O. *J. Geophys. Res. Atmos.* **2002**, *107*, ACH 14–1–ACH 14–14, DOI: 10.1029/2001JD000451.

(47) Swietlicki, E. et al. Hygroscopic properties of submicrometer atmospheric aerosol particles measured with H-TDMA instruments in various environments – A review. *Tellus B: Chem. Phys. Meteorol.* **2008**, *60*, 432–469, DOI: 10.1111/j.1600-0889.2008.00350.x.

(48) Bey, I.; Jacob, D. J.; Yantosca, R. M.; Logan, J. A.; Field, B. D.; Fiore, A. M.; Li, Q.; Liu, H. Y.; Mickley, L. J.; Schultz, M. G. Global modeling of tropospheric chemistry with assimilated meteorology: Model description and evaluation. *Journal of Geophysical Research: Atmospheres* **2001**, *106*, 23073–23095, DOI: 10.1029/2001JD000807.

(49) Grell, G. A.; Peckham, S. E.; Schmitz, R.; McKeen, S. A.; Frost, G.; Skamarock, W. C.; Eder, B. Fully coupled "online" chemistry within the WRF model. *Atmospheric environment* **2005**, *39*, 6957–6975, DOI: 10.1016/j.atmosenv.2005.04.027.

(50) Fountoukis, C.; Nenes, A. ISORROPIA II: a computationally efficient thermodynamic equilibrium model for K+–Ca 2+–Mg 2+–NH 4+–Na+–SO 4 2—NO 3—Cl—H 2 O aerosols. *Atmospheric Chemistry and Physics* **2007**, *7*, 4639–4659, DOI: 10.5194/acp-7-4639-2007.

(51) Zaveri, R. A.; Easter, R. C.; Fast, J. D.; Peters, L. K. Model for simulating aerosol interactions and chemistry (MOSAIC). *Journal of Geophysical Research: Atmospheres* **2008**, *113*, DOI: 10.1029/2007JD008782.

(52) Iacono, M. J.; Delamere, J. S.; Mlawer, E. J.; Shephard, M. W.; Clough, S. A.; Collins, W. D. Radiative forcing by long-lived greenhouse gases: Calculations with the AER radiative transfer models. *Journal of Geophysical Research: Atmospheres* **2008**, *113*, DOI: 10.1029/2008JD009944.

(53) Abdul-Razzak, H.; Ghan, S. J. A parameterization of aerosol activation: 2. Multiple aerosol types. *Journal of Geophysical Research: Atmospheres* **2000**, *105*, 6837–6844, DOI: 10.1029/1999JD901161.

(54) Shiraiwa, M.; Ammann, M.; Koop, T.; Pöschl, U. Gas uptake and chemical aging of semisolid organic aerosol particles. *Proceedings of the National Academy of Sciences* **2011**, *108*, 11003–11008, DOI: 10.1073/pnas.110304510.

(55) Kolb, C. E. et al. An Overview of Current Issues in the Uptake of Atmospheric Trace Gases by Aerosols and Clouds. *Atmos. Chem. Phys.* **2010**, *10*, 10561–10605, DOI: 10.5194/acp-10-10561-2010.

(56) Bohren, C. F.; Huffman, D. R. *Absorption and Scattering of Light by Small Particles*; Wiley, 1983.

(57) Wiscombe, W. J. Improved Mie scattering algorithms. *Appl. Opt.* **1980**, *19*, 1505–1509, DOI: 10.1364/AO.19.001505.

(58) Mayer, B.; Kylling, A. Technical note: The libRadtran software package for radiative transfer calculations – description and examples of use. *Atmos. Chem. Phys.* **2005**, *5*, 1855–1877, DOI: 10.5194/acp-5-1855-2005.

(59) Emde, C.; Buras, R.; Mayer, B.; Blumthaler, M. The libRadtran software package for radiative transfer calculations (version 2.0.1). *Geosci. Model Dev.* **2016**, *9*, 1647–1672, DOI: 10.5194/gmd-9-1647-2016.

(60) Stamnes, K.; Tsay, S.-C.; Wiscombe, W.; Jayaweera, K. A Numerically Stable Algorithm for Discrete-Ordinate-Method Radiative Transfer in Multiple Scattering and Emitting Layered Media. *Appl. Opt.* **1988**, *27*, 2502–2509, DOI: 10.1364/AO.27.002502.

(61) Gierens, K. A distribution law for relative humidity in the upper troposphere and lower stratosphere derived from in situ measurements. *Meteorol. Z.* **1999**, *8*, 83–88, DOI: 10.1127/metz/8/1999/83.

(62) Dykema, J. A.; Keith, D. W.; Keutsch, F. N. Improved aerosol radiative properties as a foundation for solar geoengineering risk assessment. *Geophys. Res. Lett.* **2016**, *43*, 7758–7766, DOI: 10.1002/2016GL069258.

(63) Vennes, B.; Bain, A.; Davies, J. F.; Preston, T. C. Optimizing stratospheric aerosol lifetime and albedo through particle morphology and refractive index. *Environ. Sci.: Atmos.* **2025**, *5*, 998–1013, DOI: 10.1039/D5EA00026B.

(64) The Royal Society *Solar radiation modification: Policy briefing*; Policy briefing, 2024; Accessed 2026-01-24.

(65) Hack, M.; McNeill, V. F.; Steingart, D.; Wagner, G. Engineering and logistical concerns add practical limitations to stratospheric aerosol injection strategies. *Sci. Rep.* **2025**, *15*, 34635, DOI: 10.1038/s41598-025-20447-2.

(66) U.S. Geological Survey Mineral Commodity Summaries 2025: Magnesium metal. U.S. Geological Survey, National Minerals Information Center, 2025; https://pubs.usgs.gov/periodicals/mcs2025/mcs2025-magnesium-metal.pdf, Accessed 2026-01-24.

(67) U.S. Geological Survey Mineral Commodity Summaries 2025: Aluminum. U.S. Geological Survey, National Minerals Information Center, 2025; https://pubs.usgs.gov/periodicals/mcs2025/mcs2025-aluminum.pdf, Accessed 2026-01-24.

(68) Fichani, K.; Teseletso, L. S.; Kaavera, J.; Dintwe, T. K.; Shemang, E.; Matshediso, B. I. The impact of junior miners on the global supply of high-purity manganese sulfate monohydrate for the electric vehicle battery market. *J. S. Afr. Inst. Min. Metall.* **2025**, *125*, 233–242, DOI: 10.17159/2411-9717/3196/2025.

(69) Wesselkaemper, J.; Thakre, P.; Ward, A.; Haddad, A. Z. Primary material supply configurations and domestic recycling for cost-effective battery material production in the US. *Nat. Commun.* **2026**, *17*, 253, DOI: 10.1038/s41467-025-66957-5.

(70) Wu, G.; Tong, H.; Liu, X.; Feng, L. Structure pattern and evolution of global magnesium trade network: An industrial chain perspective. *J. Clean. Prod.* **2025**, *524*, 146448, DOI: 10.1016/j.jclepro.2025.146448.

(71) Haywood, J.; Tilmes, S.; Jones, A.; Keutsch, F.; Laakso, A.; Niemeier, U.; Schmidt, A.; Visioni, D.; Yu, P. *Scientific Assessment of Ozone Depletion: 2022*; Global Atmosphere Watch (GAW) Report 278; World Meteorological Organization (WMO): Geneva, Switzerland, 2022; Chapter 6.

(72) Pitari, G.; Aquila, V.; Kravitz, B.; Robock, A.; Watanabe, S.; Cionni, I.; Luca, N. D.; Genova, G. D.; Mancini, E.; Tilmes, S. Stratospheric Ozone Response to Sulfate Geoengineering: Results from the Geoengineering Model Intercomparison Project (GeoMIP). *J. Geophys. Res. Atmos.* **2014**, *119*, 2629–2653, DOI: 10.1002/2013JD020566.

(73) Tilmes, S.; Visioni, D.; Jones, A.; Haywood, J.; Séférian, R.; Nabat, P.; Boucher, O.; Bednarz, E. M.; Niemeier, U. Stratospheric ozone response to sulfate aerosol and solar dimming climate interventions based on the G6 Geoengineering Model Intercomparison Project (GeoMIP) simulations. *Atmos. Chem. Phys.* **2022**, *22*, 4557–4579, DOI: 10.5194/acp-22-4557-2022.

(74) Salas, S.; Sheldon, C. S.; McMillan, K.; Palmisano, A. M.; Palacios-Diaz, T.; Morton, K.; Patel, A.; Davis, R. D.; Davies, J. F. Influence of Gel Formation on the Heterogeneous Oxidation of Organic Aerosol. *ACS Earth Space Chem.* **2025**, *9*, 2874–2884, DOI: 10.1021/acsearthspacechem.5c00302.

(75) Ullah, A.; Li, Y.; Song, M. Temperature–RH dependent viscosity of organic aerosols from 273 to 303 K: implications for global N_2O_5 uptake. *Atmos. Chem. Phys.* **2026**, *26*, 2319–2329, DOI: 10.5194/acp-26-2319-2026.

All reported measurements are provided as an .xlsx file, Sulfate_Measurements.xlsx, in the Supporting Information.